

Evaluating the Redox Behavior of Doped Ceria for Thermochemical CO₂ Splitting Using Time-Resolved Raman Spectroscopy

E. Sediva, A. J. Carrillo, C. E. Halloran, and J. L. M. Rupp*

Cite This: <https://dx.doi.org/10.1021/acsaem.0c02675>

Read Online

ACCESS |



Metrics & More



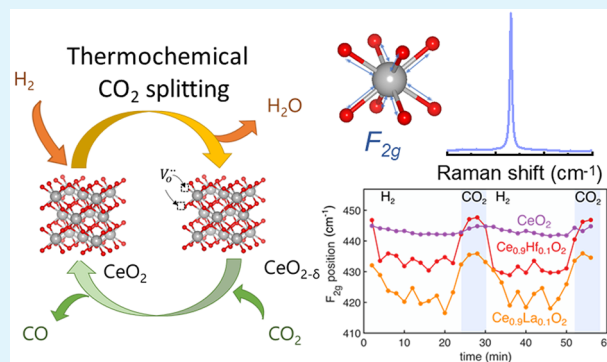
Article Recommendations



Supporting Information

ABSTRACT: Solar-to-fuel technology promises to play a key role in realizing a carbon-neutral future by enabling renewable fuel processing for capacity-independent storage beyond current battery technologies. Redox metal oxides enable the two-step thermochemical cycle at the heart of this technology by facilitating the reduction of H₂O and CO₂ to produce H₂ and CO. Currently, ceria is the material of choice for this technology; however, the low oxygen exchange capacity of CeO₂ has motivated its doping with tetravalent cations as a strategy to increase the maximum fuel yield per cycle. It is challenging to probe the defect chemical and short-range structural changes in CeO₂ during thermochemical cycling. However, these are crucial for understanding the reasons behind a material's oxygen exchange capacity and redox kinetics. To gain more insights about the effects of isovalent doping, in this work, we demonstrate how to access the defect chemical changes during fuel production by Raman spectroscopy. The results illuminate the reaction mechanisms of oxygen vacancy formation and CO₂ splitting in doped ceria solid solutions of Ce_{0.9}Hf_{0.1}O₂, undoped ceria, and trivalently doped Ce_{0.9}La_{0.1}O₂. By tracking the frequency shift of the F_{2g} mode during thermochemical cycling under oxidizing CO₂ and reducing H₂, we estimate the oxygen exchange capacity due to cation expansion and vacancy formation. We connect these results with the fuel production performance of these materials in a fixed-bed reactor and corroborate the kinetic effects of +3 and +4 doping. The methodology presented here could be extrapolated to other redox systems used for thermochemical syngas production and energy conversion, such as chemical looping combustion or electrochemical fuel production, proving fundamental insights into vacancy formation that could be useful in the design of new materials and understanding reaction pathways.

KEYWORDS: CO₂ splitting, *in situ* Raman, doped ceria, thermochemical cycles, solar fuels



1. INTRODUCTION

Solar-driven thermochemical syngas production is an auspicious technology that transforms the most abundant renewable resource on earth into synthetic fuels and has the potential to contribute to the decarbonization of the energy sector.¹ The solar-to-fuel scheme discussed in this paper consists of a two-step redox reaction of a metal oxide to convert solar energy, CO₂, and H₂O into syngas, which can be further transformed into liquid fuels by the Fischer–Tropsch process.² In the first step, concentrated solar power (Figure 1) is utilized to drive the thermal reduction of the metal oxide at high temperatures (1100–1500 °C), liberating lattice oxygen (eq 1).



In the case of nonstoichiometric oxides, for example, ceria and perovskites, this process is associated with the generation of oxygen vacancies. The reduction extent, or the change in the material's oxygen nonstoichiometry δ , denotes the amount of oxygen vacancies created in this first process. In the second

step, a gaseous stream of CO₂, H₂O, or a mixture thereof is injected into the solar reactor, refilling the oxygen vacancies and generating CO (eq 2a) and H₂ (eq 2b).³



Here, the stoichiometry of both the CO₂ and H₂O splitting reactions dictates that the amount of fuel produced is proportional to δ , the amount of vacancies generated in the previous half-cycle step. This stoichiometric relationship highlights the importance of finding redox materials with

Received: October 28, 2020

Accepted: January 15, 2021

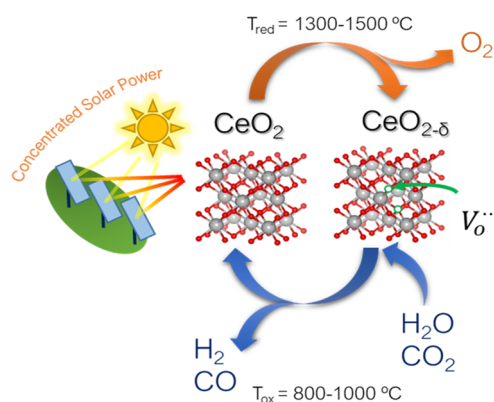


Figure 1. Schematic of the two-step solar-driven thermochemical fuel production based on ceria redox cycles.

high oxygen exchange capacity and the thermodynamic ability to split CO_2 and H_2O .

The state-of-the-art material is ceria due to its favorable thermodynamics for H_2O and CO_2 splitting, fast splitting kinetics, and high-temperature stability that allows continuous cycling without degradation.^{4–7} Research on nonstoichiometric thermochemical cycles of ceria has been an active research topic during the past decade with major breakthroughs.⁸ For instance, the viability of the entire solar to liquid fuels (kerosene) process was demonstrated by using a reticulated porous structure of ceria placed inside a cavity reactor and utilizing a solar simulator as radiation source.⁹ To improve the efficiency of this process, the same authors showed that applying vacuum during the reduction step increased the extent of reduction, leading to a 5.25% solar-to-fuel efficiency, which is the highest to date.¹⁰ Despite the promise of these results, ceria still shows inherent drawbacks related to the amount of oxygen vacancies that can be created, which directly correlates with the fuel production. To address this limitation, several strategies have been used such as changes in the textural properties,¹¹ processing as dual phase composites^{12–17} or cationic metal doping.^{18,19} This latter approach has been extensively explored to create intrinsic oxygen vacancies for enhancing the fuel yield. Additionally, chemical modifications of ceria's fluorite structure by partial substitution of Ce^{4+} can decrease the high reduction temperature (1400–1500 °C) of ceria. However, this substitution should be conducted carefully because a decrease in the reduction temperature is normally associated with a decrease in the enthalpy of reduction and might lead eventually to a decrease on the process efficiency.²⁰

A plethora of dopants have been studied for improving the redox properties of ceria, oxygen vacancy (δ) formation, and

fuel production; most research has focused on the partial substitution of Ce^{4+} by Zr^{4+} ^{21–25,18,26} and other tetravalent dopants. Indeed, Jacot et al. screened 26 tetravalent dopants, assessing their stability and oxygen exchange.²⁶ They found that Zr, Hf, Pr, and Tb were the most thermally stable when doping up to 10 mol %. In addition, they empirically established that the ideal dopant ionic radii for optimum oxygen exchange capacity is around 0.8 Å.²⁶ However, the increased reduction extent from incorporating Zr^{4+} and Hf^{4+} comes at the price of slower reoxidation kinetics compared to pure ceria.^{21,24} Contrarily, trivalent doping could increase the redox kinetics because it induces the formation of stable oxygen vacancies¹⁸ that enhance the ionic conductivity, whereas tetravalent doping induces the formation of reversible vacancies.

Despite these facts, the way in which both types of vacancies interact during the cyclic thermochemical process for fuel generation is still poorly understood. A promising tool to tackle this lack of information and shed more light into the role of oxygen vacancies in thermochemical processes is *in situ* Raman spectroscopy,²⁷ which has been established as a powerful tool to study redox changes and defect chemistry in ceria-based materials.^{28–32} Especially, Raman spectroscopy has been found very useful for estimating the oxygen vacancy concentration,^{28,33–35} for instance by converting the red-shift of the main Raman mode into a change in oxygen nonstoichiometry based on expansion during reduction.³⁰

The Raman spectrum of CeO_2 is dominated by the only Raman-active F_{2g} band at 465 cm^{-1} , which corresponds by symmetry analysis to a symmetrical stretching of oxygen around the Ce^{4+} cation (Figure 2a). However, we should note that the $\text{Ce}^{4+}\text{--O}$ and the O--O force constant contribute to this Raman band.³⁶ Doping with trivalent and tetravalent cations gives rise to extra defect bands in the Raman spectrum around 540 and 600 cm^{-1} , often labeled as D_1 and D_2 . These are usually respectively attributed to a defect space containing a dopant atom and oxygen vacancies. In some studies the area ratio between the vacancy-induced band (D_2) and the F_{2g} mode is used as a measure for the oxygen vacancy concentration, reported also in *in situ* studies illuminating defect-chemical properties of ceria-based materials under various atmospheres and temperatures.^{35,37} However, Raman studies on how these modes change under cyclic solar-to-fuel conditions, and their correlation with the redox kinetics and fuel yields is so far missing.

For this reason, in this work, we investigate the redox properties of ceria by establishing the roles of oxygen vacancies in fuel production rate and yield, driven by the incorporation of trivalent or tetravalent dopants. For this purpose, we

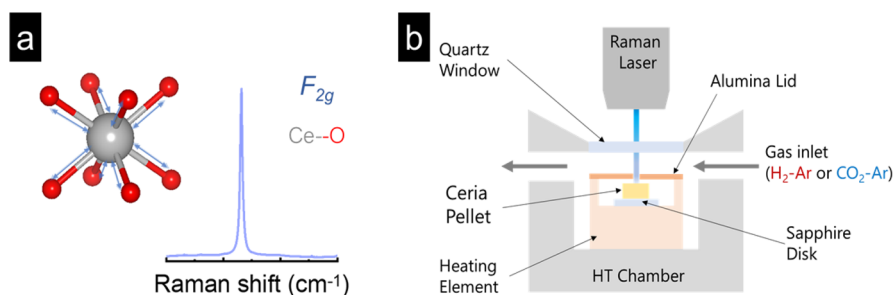


Figure 2. (a) Representation of the symmetrical stretching of oxygen around the Ce^{4+} cation F_{2g} Raman mode on ceria. (b) Schematic of the high-temperature chamber setup utilized for *in situ* Raman tests.

synthesized the compositions $\text{Ce}_{0.9}(\text{Me})_{0.1}\text{O}_2$ with tetravalent $\text{Me} = \text{Hf}$ and trivalent $\text{Me} = \text{La}$ dopants and compare these to the benchmark undoped CeO_2 . We measure the changes in the F_{2g} and the defect-induced modes during the reduction and fuel production steps. We estimate the changes in the oxygen stoichiometry based on a model of chemical expansion and connect these to the fuel production yields from the fixed bed reactor. With this study we aim to establish Raman spectroscopy as a valuable tool to study the structural and redox properties of ceria-based materials under thermochemical solar-to-fuel conversion conditions.

2. EXPERIMENTAL METHODS

2.1. Materials Preparation. Tetravalently and trivalently doped ceria materials were prepared for Raman spectroscopy and thermochemical cycling analysis: $\text{Ce}_{0.9}(\text{Me})_{0.1}\text{O}_2$ with $\text{Me} = \text{La}, \text{Hf}$. In addition, a commercial sample of pure ceria (CeO_2 , Sigma-Aldrich, 99.0%) was used as a benchmark. To achieve homogeneous, phase-pure samples of the doped materials, a modified Pechini method was used to synthesize powders of each material. Cerium nitrate ($\text{Ce}(\text{NO}_3)_3 \cdot 7\text{H}_2\text{O}$, 99.99%, Alfa Aesar) and a nitrate or chloride salt of the dopant cation(s) ($\text{La}(\text{NO}_3)_3 \cdot 6\text{H}_2\text{O}$, 99.9%, Alfa Aesar, and HfCl_4 , 99.9%, Alfa Aesar) were combined in the desired stoichiometric ratio in aqueous solution with citric acid in a 3:2 molar ratio of citric acid to the nitrate salts. After this solution was heated to 80 °C, ethylene glycol was also added in a 2:3 mass ratio to citric acid to form a polypeptide organic matrix to ensure the uniform distribution of the doped ceria precursors. This solution formed a gel and then a foam as the organic matrix formed. The resulting foam was then burnt off on a hot plate at 400 °C, leaving behind a fine powder of substituted ceria. This powder was then ground and sintered in a box furnace at 1200 °C for 5 h. Finally, the samples (CeO_2 , $\text{Ce}_{0.9}\text{La}_{0.1}\text{O}_2$, and $\text{Ce}_{0.9}\text{Hf}_{0.1}\text{O}_2$) were shaped into small pellets of ca. 1 mm thickness for the Raman experiments by using a hydraulic press under 2.5 tons of pressure for 120 s. The pellets were then sintered for an additional 5 h at 1400 °C. For the fixed-bed reactor tests commercial CeO_2 was used as received without further treatment.

2.2. XRD Phase Confirmation. To confirm the fluorite phase purity of the samples, the as-synthesized doped-ceria materials were analyzed by X-ray powder diffraction using a Panalytical X'Pert PRO MPD diffractometer. Cu K α radiation ($\lambda = 1.54178 \text{ \AA}$) produced with an extraction voltage of 45 kV at 40 mA current was used to scan the samples in a Bragg–Brentano geometry in the range of $20^\circ < 2\theta < 120^\circ$ with a spinning speed of 60 rpm, a step width of 0.017° , and an irradiation time of 3 s. Cell parameters were obtained by Rietveld refinement using Panalytical HighScore Plus software.

2.3. Raman Spectroscopy. The Raman spectra were collected with a confocal WITec alpha300 R Raman microscope (WITec, Germany). The laser excitation wavelength was 457 nm (2.71 eV), the laser power 1.5 mW, the grating 1800 grooves/mm, and the objective 50 \times with a numerical aperture of 0.7 (Zeiss, Germany). These conditions give a spectral resolution of 0.53 cm^{-1} and an approximate laser spot size of 1 μm . The Raman modes were fit with a Lorentzian function by using the WITec Suite FOUR software.

2.4. CO₂ Splitting Reactor Tests. The fuel production ability of synthesized doped-ceria samples was tested in a fixed-bed high-temperature reactor described elsewhere.³⁸ Each sample (ca. 0.25 g) was subjected to three redox thermochemical cycles with conditions similar to the Raman tests for the sake of comparison. Reduction was performed under 10% H₂ for 20 min and oxidation under 50% CO₂ for 5 min at 800 °C with a total gas flow of 300 mL min^{-1} . The gas compositions were monitored with a Raman laser gas analyzer from Atmospheric Recovery Inc.

Here we want to note that ideally reduction is meant to be thermally driven by concentrated solar radiation. However, for our study, we choose to chemically reduce the sample for two reasons. First, it lowers the reduction temperature from 1400 to 1500 to 800 °C, which is beneficial for the interpretation of Raman spectra because

high temperatures negatively affect band intensity and resolution. Second, the lower pO₂ leads to a higher concentration of oxygen vacancies at lower temperatures, which might be also positive for interpretation of the *in situ* Raman results. Additionally, the extent of reduction in H₂ can be comparable to reduction with other fuels such as CH₄,^{22,23,39} which can be very useful for researchers working in solar fuel production via chemical looping reforming⁴⁰ or reverse water-gas shift chemical looping (RWGS-CL).⁴¹

2.5. Raman Spectroscopy under Redox Cycling. For Raman measurements at high temperatures a Linkam HT1500 (Resultec, Germany) stage was utilized, and a schematic of the setup is depicted in Figure 2b. The high-temperature stage was connected to a T95-LinkPad system controller, which allows fast heating to $200 \text{ }^\circ\text{C min}^{-1}$. The ceria-based pellets were placed over a 0.3 mm sapphire disk inside the ceramic micro-oven located inside the Linkam chamber and covered with a perforated alumina lid shield that prevented heat losses. Temperature was controlled with a Type S Pt-10% Rh/Pt thermocouple, with a temperature stability of 1 °C. Finally, the chamber was tightly closed with a metallic lid with a 1 mm quartz window to allow the Raman laser to impinge the oxide pellet. Reducing (10% H₂ balanced with Ar 99.999% pure both from Airgas) or oxidizing gas streams (10% CO₂ balanced with Ar both from Airgas) were delivered at a total flow rate of 50 mL min^{-1} to the Linkam stage by using a set of electronic mass flow controllers from Voegtlin.

Tests were performed to analyze the impact of thermochemical redox cycles on the Raman spectra by applying two reducing–oxidizing chemical loops to the cerium-based oxides at 800 °C. Traditionally, chemical loops for CO₂ splitting of ceria are performed at 900–1000 °C⁴² to allow fast CO₂ splitting kinetics; however, we intentionally lowered the temperature of our study to 800 °C and used a relatively low CO₂ concentration (10 vol %) to slightly slow the CO₂ splitting kinetics^{39,43} and improve the time resolution of the Raman spectra changes. Before acquiring the spectra, the temperature inside the chamber was raised to 800 °C under an Ar atmosphere and held at these conditions for 5 min to stabilize the temperature. After that, the sample was reduced for 20 min, and spectra were acquired at 2 min intervals with a 15 s integration time for each acquisition. Following that step, Ar was injected for 2 min to purge the reducing gas before CO₂ injection. Oxidation was performed for 6 min while spectra were acquired at 2 min intervals. This redox sequence was repeated two times.

3. RESULTS AND DISCUSSION

We selected dopants with 3+ (La) and 4+ (Hf) valence for ceria as they present a model system for analyzing the effects of trivalent and tetravalent doping in solar to fuel conversion.^{24,44,45} For this, $\text{Ce}_{0.9}\text{Me}_{0.1}\text{O}_{2-\delta}$ with $\text{Me} = \text{La}, \text{Hf}$ powders were synthesized by the Pechini method. Both synthesized materials and commercial CeO_2 (Sigma-Aldrich) exhibited cubic fluorite crystal structure space group *Fmm3* as analyzed by XRD (Figure 3) with the main representative diffraction peak (111) located at ca. 28.5°. The lattice volume was determined by Rietveld refinement from XRD data obtained at room temperature and air atmosphere. An example Rietveld refinement fit for CeO_2 can be found in the Supporting Information (Figure S1). Partial substitution of Ce^{4+} by the tetravalent cation Hf^{4+} resulted in lattice shrinkage due to the smaller ionic radius of 0.83 Å compared with that of Ce^{4+} in 8-fold coordination, 0.97 Å.⁴⁶ Hf-doped ceria samples exhibited lattice volumes 155.83 \AA^3 , whereas the lattice volume for CeO_2 is 158.2 \AA^3 . Conversely, incorporation of a trivalent cation, La^{3+} , resulted in lattice expansion to 161.7 \AA^3 due to its larger ionic radius of 1.16 Å. The effects on the lattice caused by incorporation of both dopants match well with previous reports.⁴⁵ We conclude that the synthesis was successful

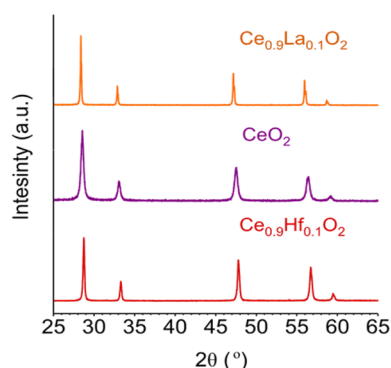


Figure 3. X-ray diffraction patterns of the as-synthesized La- and Hf-doped ceria materials and the as-received commercial CeO₂.

obtaining solid solutions both La- and Hf-doped ceria materials and avoiding the presence of secondary phases.

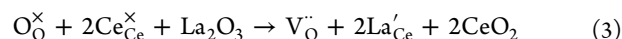
Now we turn to the analysis of the CO₂ splitting ability of each material, which was studied in a fixed-bed high-temperature reactor. Materials were subjected to a three-cycle test, in which reduction was performed with 10% H₂ to match the conditions of the Raman test (see the [Experimental Methods](#)). [Figure 4](#) depicts the CO production rate curves during CO₂ splitting at 800 °C, exemplified for the second cycle.

The tetravalent dopant of Hf shows the highest CO production, while the trivalent La-doped ceria only slightly improves the production of undoped ceria. The strong fuel production performance of the tetravalent dopant suggests that oxygen vacancies, the formation of which is made more energetically favorable by the tensile strain in Hf–O bonds,⁴⁷ play a key role in CO₂ splitting. In contrast, doping CeO₂ with trivalent rare earths has been shown to decrease the fuel yields during thermochemical cycling,^{44,48} which is corroborated by the presently measured low yields of the La-doped CeO₂. Large trivalent dopant cations like La show lower associations with oxygen vacancies because the local relaxation around the vacancy is impeded by their large size, lower valence, and the presence of extrinsic oxygen vacancies. Because of the unfavorable reduction around the trivalent dopant cation, the number of sites (Ce⁴⁺–O₈) available for reduction also decreases. Therefore, generally dopants with the 4+ valence and small ionic radii were shown to be beneficial for thermochemical cycling.⁴⁹

When examining the kinetics of the fuel production step, the CO production peak ([Figure 4](#)), we notice that the La-doped

ceria shows the fastest reaction rates, followed by undoped CeO₂ and Ce_{0.9}Hf_{0.1}O₂. Therefore, the reaction rates show the opposite behavior compared to the fuel yields. This agrees with the work of Jacot et al.,²⁶ who indicated that trivalent dopants favor the creation of inactive oxygen vacancies that improve the ionic conductivity and, in turn, the CO₂ splitting kinetics. For Ce_{0.9}Hf_{0.1}O₂, the decrease on the reoxidation rate, compared to ceria, has been previously reported by Scheffe et al.²⁴ Both Zr and Hf tetravalent dopants have been found to increase the reduction extent at the expense of worse oxidation kinetics. The increase on the reduction extent is explained by the decrease on the reduction enthalpy when doping with tetravalent dopants. However, lowering the reduction enthalpy also decreases the driving force for the oxidation reaction, which might affect also to the slow oxidation kinetics.^{50,51}

3.1. Room Temperature Raman Spectroscopy of Ce_{0.9}M_{0.1}O_{2-δ}. It is crucial to understand the Raman spectra of the ceria-based materials to link the Raman mode positions and intensities to chemical and physical changes in the materials. In pure CeO₂ we observe a single band at 464 cm⁻¹ ([Figure 5a](#)), which we ascribe to the F_{2g} mode in agreement with earlier literature.^{27,34} This is the only Raman-active mode of pure cubic ceria and corresponds to the symmetric stretching of eight oxygen anions around the Ce⁴⁺ cation. With the addition of dopant cations, the F_{2g} mode shifts in wavenumber and decreases in intensity, and additional modes appear in the spectrum ([Figure 5b](#)), which implicate local lowering of symmetry (see [ref 27](#) for details). The F_{2g} mode shifts to lower wavenumbers with increasing dopant cation size and lattice volume ([Figure 5c](#)). This is in accordance with previous literature results^{27,29} and can be ascribed to a vibrational frequency decrease coupled to lattice volumetric expansion. In Ce_{0.9}La_{0.1}O_{2-δ}, three additional modes appear at 252 (see also [Figure S2](#)), 533, and 583 cm⁻¹ and in Ce_{0.9}Hf_{0.1}O_{2-δ} at 586 and 620 cm⁻¹. These modes also decrease their vibrational frequency with the cation radius ([Figure 5d](#)), signifying lattice expansion. They are generally considered to be activated by symmetry lowering defects,^{28,29} namely oxygen vacancies and the dopant cations. Charge compensating, or extrinsic, oxygen vacancies form in the trivalently doped CeO₂ (in Kröger–Vink notation)



Additionally, at temperatures above about 900 °C, the reduction of Ce⁴⁺ results in the formation of intrinsic oxygen vacancies.

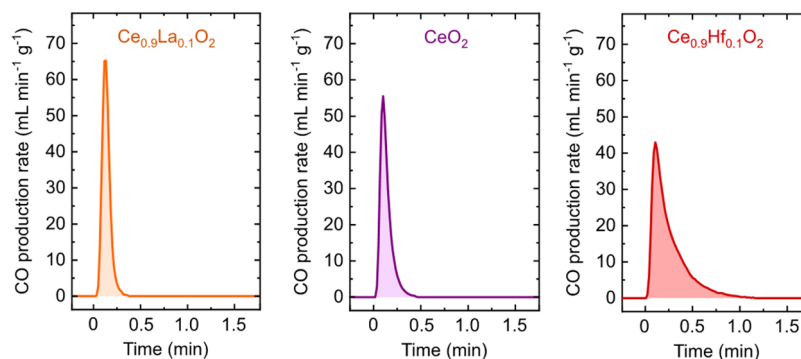


Figure 4. CO production rate curves from CO₂ splitting tests (50% CO₂, 5 min) at 800 °C of Ce_{0.9}La_{0.1}O₂, CeO₂, and Ce_{0.9}Hf_{0.1}O₂. Materials were previously reduced for 20 min with 10% H₂ balanced in Ar at 800 °C.

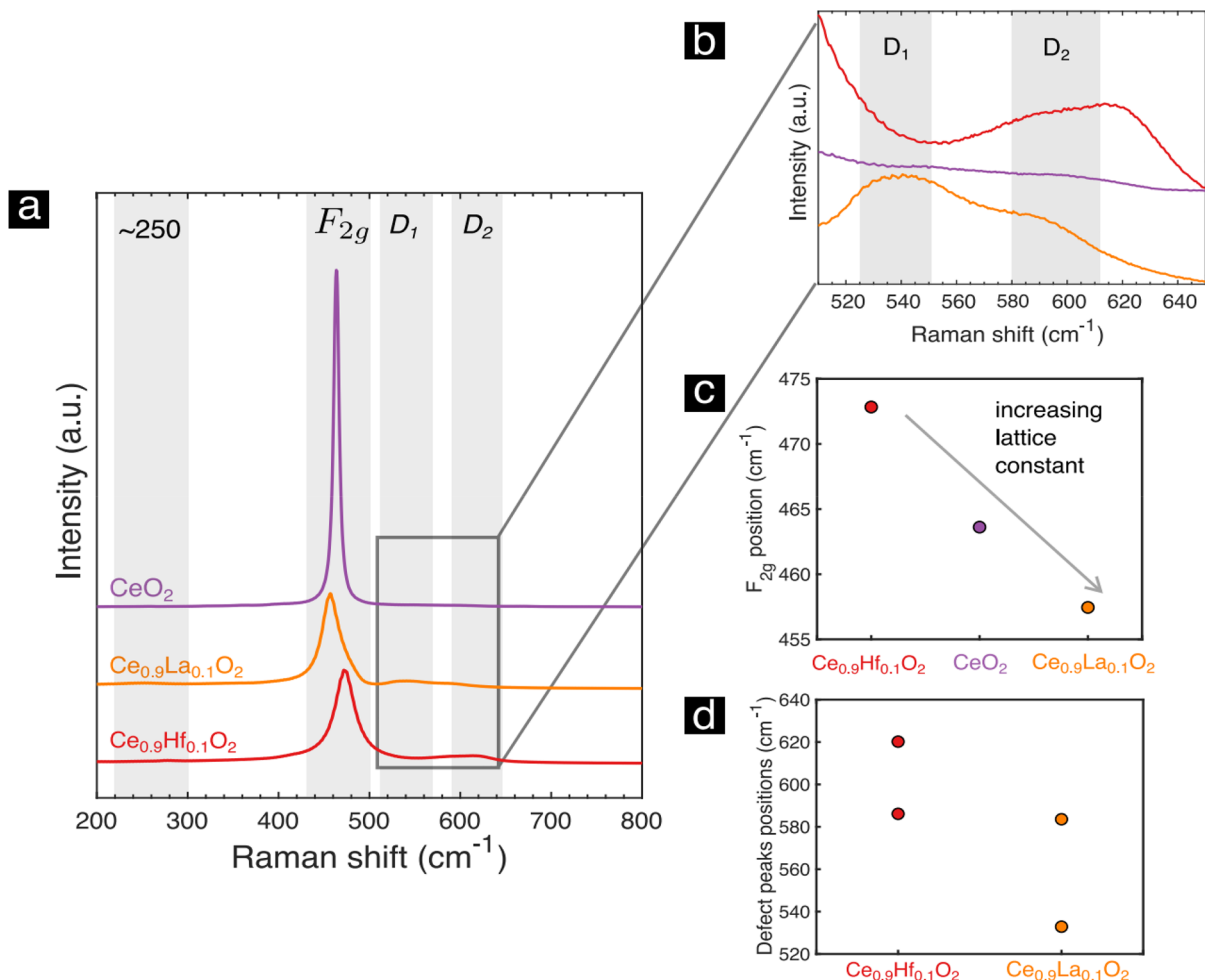


Figure 5. Room temperature Raman spectroscopy. (a) Full Raman spectra of CeO₂, Ce_{0.9}La_{0.1}O_{2-δ}, and Ce_{0.9}Hf_{0.1}O_{2-δ} at room temperature. (b) Zoom-in of the Raman spectra in (a) emphasizing the modes that emerge with doping. (c) Fit of the F_{2g} Raman mode as a function of the dopant cation. (d) Defect band positions.



For the Raman defect mode assignment (Figure 5b,d), we follow the study of Nakajima et al. and attribute the mode around 530 cm⁻¹ (D₁) in the spectrum of La-doped ceria to vibrations in a defect space including an oxygen vacancy and the mode close to 600 cm⁻¹ (D₂) present in the spectra of both La- and Hf-doped ceria to vibrations including the dopant cation.²⁸ Here we would like to point out that also other interpretations of the defect bands have been proposed,⁵² and their assignment is therefore still a matter of debate. Interestingly, the Ce_{0.9}Hf_{0.1}O₂ spectrum shows two broad bands in the region of 600 cm⁻¹ where only one D₂ mode is expected from vibrations that include the dopant ion.⁵³ It is not clear why this band splitting occurs, but it could signify an additional symmetry break. This could be, for example, a slight tetragonality, which is known to occur in ceria–zirconia compounds.⁵⁴ Lastly, we observe that with the addition of dopant cations, the F_{2g} mode broadens and decreases in intensity, as can be observed in Figure 5a. We attribute the larger width of the band to the disorder induced by the dopant cations and oxygen vacancies. The lower intensity is a result of the higher absorption coefficients of the substituted materials and the lower overall number of Ce⁴⁺–O₈ complexes. Figure 6 summarizes the performance of each material in the fixed bed

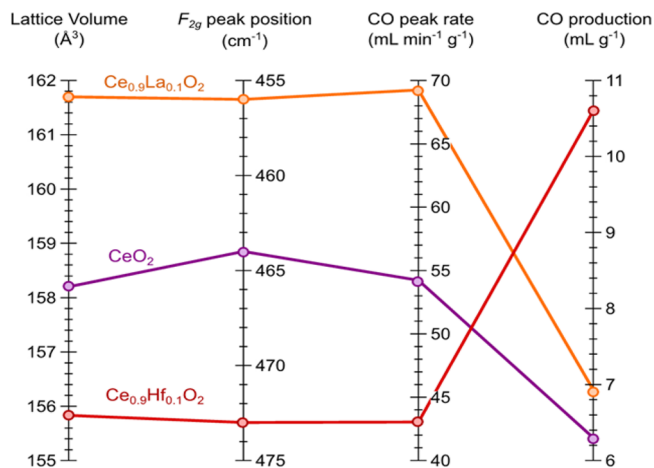


Figure 6. Lattice volume, F_{2g} Raman peak position, CO peak rate, and CO production for CeO₂, Ce_{0.9}La_{0.1}O_{2-δ}, and Ce_{0.9}Hf_{0.1}O_{2-δ}.

reactor, depicting the peak CO production rate and overall CO yield per gram of catalytic material in the second cycle and its relationship with the crystal lattice volume. Trivalent doping, in this case with La³⁺, induces lattice expansion, as confirmed by XRD and Raman spectroscopy, and presents the fastest kinetics for CO₂ splitting. On the other hand, tetravalent

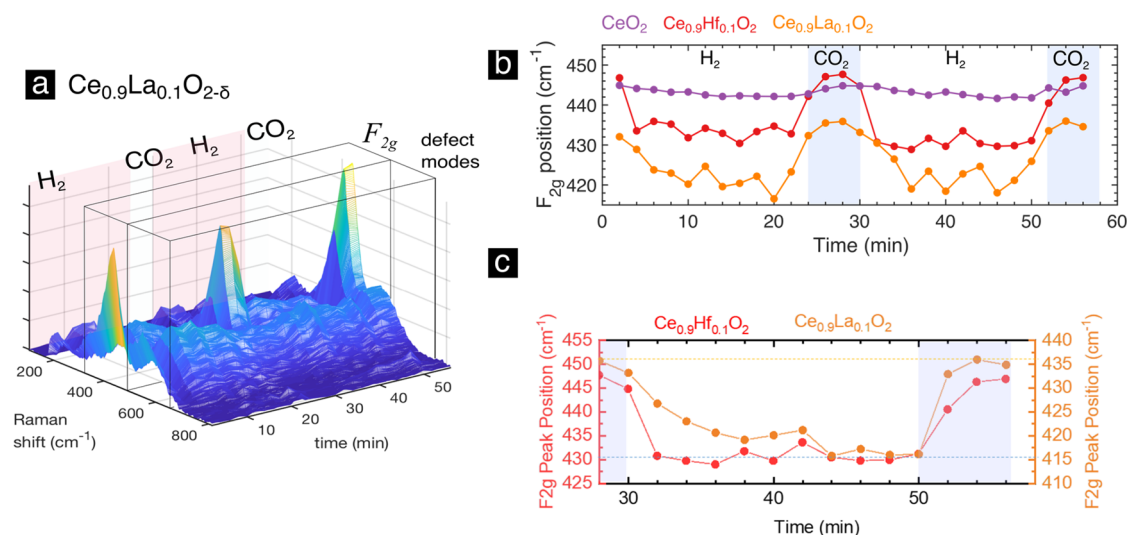


Figure 7. Time-resolved Raman spectroscopy measurements performed at 800 °C. (a) Example time evolution of the full Raman spectra over two thermochemical cycles in a three-dimensional representation. For each cycle, reduction was performed in a 10% H₂ atmosphere for 20 min and subsequent oxidation under a 10% CO₂ atmosphere, both balanced with Ar at a total flow rate of 50 mL min⁻¹. (b) F_{2g} band position as a function of time. (c) Zoom-in of (b) for comparing the oxidation kinetics of Hf- and La-substituted ceria.

doping causes lattice shrinkage, favoring an increase in CO production, but at more moderate rates.

We now understand the Raman spectral changes in ceria-based materials during lattice volume expansion and generation of oxygen vacancies, which both accompany the reduction of ceria,⁵⁵ a critical process in thermochemical cycling. Therefore, we can next turn to the *in situ* thermochemical cycling results.

3.2. Raman Spectroscopy under Thermochemical Cycling. Raman spectral changes during two oxidation and reduction cycles are shown in a three-dimensional representation in Figure 7a for Ce_{0.9}La_{0.1}O_{2-δ}. Immediately noticeable is the decrease in the intensity and area of the F_{2g} Raman mode during reduction. We attribute it to the increase of the absorption coefficient during reduction as well as to the increasing disorder and decreasing amount of Ce⁴⁺-O₈ complexes as oxygen vacancies and Ce³⁺ are introduced. It is also consistent with the decrease in the F_{2g} intensity in the La- and Hf-doped CeO₂ (Figure 5a), which was also corroborated in previous studies where the F_{2g} band area decreases with increasing levels of substitution in ceria.⁵⁶ During the thermochemical cycling, we could successfully track the F_{2g} band position in all the considered materials (Figure 7b). We observe the expected decrease in the vibrational frequency during reduction as the material expands and an increase during oxidation as the material contracts. We estimate the changes in oxygen nonstoichiometry during the thermochemical cycling with the help of the chemical expansion⁵⁵ and Raman chemical shift constant⁵⁷ concepts, detailed in the Supporting Information. We calculate the maximum difference in the oxygen nonstoichiometry Δδ during cycling of 0.18, 0.03, and 0.2 for Ce_{0.9}Hf_{0.1}O₂, CeO₂, and Ce_{0.9}La_{0.1}O₂, respectively (see also Figure S3). The calculated changes in the oxygen nonstoichiometry are very high, especially for the Hf- and La-doped CeO₂. At these high oxygen vacancy concentrations, the interaction between the defects is unavoidable, and the presence of defect associates and especially intrinsic (Ce_{Ce}V_OCe_{Ce})^{58,59} and extrinsic (Ce_{Ce}V_OLa_{Ce}La_{Ce}V_OLa_{Ce}) trimers can dominate the defect

chemistry. Also at these high substitution levels of Ce³⁺, local phase changes and corresponding changes in coordination numbers can occur.⁶⁰ The chemical expansion model does not account for defect associates, and therefore the oxygen nonstoichiometry changes in both Hf- and La-doped CeO₂ are most likely overestimated.

The results from the fixed bed reactor (Figure 4) show that Ce_{0.9}Hf_{0.1}O₂ has a much higher fuel yield than CeO₂ and Ce_{0.9}La_{0.1}O₂. This should be reflected in a higher oxygen storage capacity during thermochemical cycling for Ce_{0.9}Hf_{0.1}O₂. However, the Raman spectral analysis based on chemical expansion shows the largest vibrational changes in the F_{2g} frequency in the La-doped sample, which shows little improvement in CO yield compared to the pure material in the reactor tests. The low fuel yields in Ce_{0.9}La_{0.1}O₂ are corroborated by the low reduction extent of the material, which is exemplified by the low water production during the hydrogen reduction step (Figure S4). We identify two possible reasons for the discrepancy between the Raman spectral results and the fuel yield in Ce_{0.9}La_{0.1}O₂. First, the chemical expansion model for interpreting the Raman spectral changes does not apply in the case of La-doped CeO₂, or certain oxygen vacancies formed in Ce_{0.9}La_{0.1}O₂ undergo parallel redox reactions and do not participate in the water production (Figure S4) or fuel production processes (Figure 4). The former explanation could hold if La-doped ceria had much larger chemical expansion coefficients than undoped CeO₂, leading to larger shifts in the oxygen vibrational properties. However, this is not corroborated by experimentally determined chemical expansion coefficients α_c(La:CeO₂) ≈ 0.50, α_c(CeO₂) ≈ 0.55.⁵⁵

The reason for the discrepancy between the Raman spectral results and oxygen storage capacity in Ce_{0.9}La_{0.1}O₂ therefore remains unclear. However, we could confirm with the *in situ* Raman tests the kinetic trends observed in the fixed bed reactor. Figure 4 show that La-doped ceria exhibits fast CO₂ splitting kinetics and slow oxygen release (vacancy formation), whereas the opposite is true for Hf-doped ceria. To corroborate that trend, we zoom into Figure 7b as Figure 7c.

There, we are depicting the second redox cycle performed *in situ* in the high-temperature Linkam chamber. It can be observed that under H_2 reduction Hf-doped ceria takes a shorter time to reach the lower F_{2g} band shift value, which relates to the highest reduction stage. Conversely, La-doped ceria needs longer time, about the entire reduction period, to reach the highest extent of reduction, denoting a more prolonged reduction. This connects well with the H_2O release trends obtained in the fixed bed reactor (Figure S4). There it can be seen that Hf-doped exhibits a faster reduction, with the H_2O production peak rate of ca. $5.5 \text{ mL min}^{-1} \text{ g}^{-1}$, whereas La-doped presents a steadier H_2O production curve, with a maximum of ca. $1.8 \text{ mL min}^{-1} \text{ g}^{-1}$. Once the gas is changed to CO_2 , it can be seen in Figure 7c that for La-doped ceria the first scan under the oxidizing atmosphere shows a F_{2g} band value of 432.9 cm^{-1} , very close the initial oxidized value before reduction, 433.1 cm^{-1} , illustrating the fast oxidation kinetics for La-doped ceria. However, for Hf-doped, the first scan under reoxidizing conditions is 440.8 cm^{-1} , whereas the value before reduction is 444.8 cm^{-1} , indicating slower CO_2 -splitting rates. These results illustrate the faster kinetics of La-doped ceria for CO_2 splitting compared to Hf-doped ceria, which takes a longer time to reach the F_{2g} band values that correspond to the oxidized state. It is important here to note that the kinetic comparison is exclusively made on a qualitative basis. The high-temperature Linkam stage has a configuration that adds external hurdles to mass transport from the gas phase to the material because, first, there is an alumina lid needed to prevent radiation losses (Figure 2b) and, second, the materials are pressed into pellet form. On the other hand, the fixed bed reactor was designed to avoid any mass transport hurdles, and samples were tested in powder form. However, the fact that by *in situ* Raman measurements the kinetic trends are corroborated is a good indicator that is a promising tool for this technology and could benefit from more optimized configurations. In addition, coupling *in situ* Raman measurements with gas monitoring unit, such as a mass spectrometer, will enable *operando* experiments providing additional insights into the reaction mechanisms and rates. This approach, also called Raman spectrokinetics,⁶¹ has recently gained attention in the catalysis community and illustrates the relevance of this study for catalytic systems that use CeO_2 and doped- CeO_2 oxides as supports,⁶² membranes for CO_2 reduction,⁶³ or chemical looping reforming of methane.⁶⁴

Next we turn to the evolution of the defect activated modes during thermochemical cycling. Because of the high spectral noise at $800 \text{ }^\circ\text{C}$, it was not possible to reliably fit two peaks representing the D_1 and D_2 Raman modes in the defect mode region between 500 and 650 cm^{-1} . The D_2 Raman mode is attributed to the vibration in the MeO_8 complex, where Me represents the dopant atom. The number of MeO_8 complexes decreases with increasing number of vacancies, and therefore the D_2 Raman mode can diminish in intensity with large oxygen vacancy concentrations. Following this reasoning, we fit only a single Lorentzian in the defect mode region, and Figure 8a shows the evolution of this band for each dopant. In Hf-doped CeO_2 we observe a frequency increase during oxidation to about 590 cm^{-1} . Also, the band area increases during reduction as shown in Figure 8b. This could signify that the band is associated with the defect space for a vacancy during reduction (D_1) and a defect space with the doping cation during oxidation (D_2). Interestingly, the trend for La-doped CeO_2 is opposite, and the band in the defect region increases

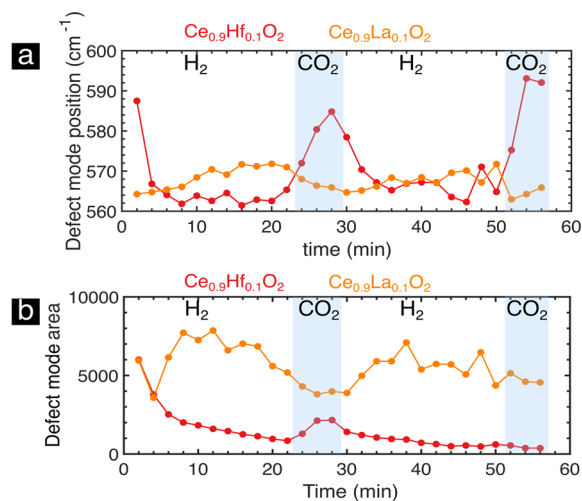


Figure 8. (a) Position of the defect activated band as a function of time for two consecutive thermochemical cycles. (b) Comparison of the area under the defect mode for the two different dopant cations: Hf and La.

in frequency during reduction, which is opposite to the trend expected from chemical expansion and the trend observed in the shift of the F_{2g} band position during cycling. Additionally, the defect activated band area of $Ce_{0.9}La_{0.1}O_{2-\delta}$ increases during reduction, opposite to $Ce_{0.9}Hf_{0.1}O_{2-\delta}$ (Figure 8b). This strongly suggests that the defect mode for $Ce_{0.9}La_{0.1}O_{2-\delta}$ is of a different origin than the mode in $Ce_{0.9}Hf_{0.1}O_{2-\delta}$. The increase in the mode area during reduction can signify it is linked to the presence of oxygen vacancies. The opposite shift in the vibrational frequency of the F_{2g} and the defect mode (D_2) in $Ce_{0.9}La_{0.1}O_{2-\delta}$ signifies an expansion of the average (global) lattice constant with a local contraction around the complex including an oxygen vacancy. One explanation could be the buildup of intrinsic ($Ce'_{Ce}V_{O}Ce'_{Ce}$) or extrinsic ($Ce'_{Ce}V_{O}La'_{Ce}La'_{Ce}V_{O}La'_{Ce}$) trimers, which are smaller than isolated oxygen vacancies⁵⁹ and could be the reason for a local lattice contraction. However, this hypothesis does not explain the lower fuel yields of $Ce_{0.9}La_{0.1}O_{2-\delta}$ when compared to $Ce_{0.9}Hf_{0.1}O_{2-\delta}$ because the large vibrational shifts in the F_{2g} mode still signify large changes in the oxygen vacancy concentration during thermochemical cycling according to the chemical expansion model.

4. CONCLUSIONS

In this work, we have evaluated the potential of *in situ* Raman spectroscopy in the field of thermochemical cycles for fuel production by using CeO_2 as reference material. We selected La- and Hf-doped ceria materials as model cases to study the influence of tri- and tetravalent doping on the formation and regeneration of oxygen vacancies by using time-resolved Raman spectroscopy under thermochemical cycling conditions at $800 \text{ }^\circ\text{C}$. This approach has so far been unexplored for redox cycles of CO_2 splitting and allows quick access to information related to the defect chemistry and redox kinetics.

Overall, we confirm the results obtained by using a packed bed reactor with the time-resolved Raman spectra corroborating that the tetravalent Hf dopant gives the highest fuel yield. This result is consistent with previous literature reports and indicates that single, intrinsic oxygen vacancies, facilitated by tetravalent doping, determine the fuel yield. In trivalent-doped

ceria ($\text{Ce}_{0.9}\text{La}_{0.1}\text{O}_2$), extrinsic oxygen vacancies that compensate for lower-valent dopant do not participate in fuel production; however, they increase the kinetics of fuel production by enhancing oxygen transport through the lattice during CO_2 splitting. Hence, we can confirm that compared to classic high-temperature reactor studies in solar-to-fuel conversion, where often changes in the ceramic in terms of nonstoichiometry are only measurable by gas production, *in situ* Raman spectroscopy can provide insights into ceria's defect chemistry during thermochemical operation. Further works in which the suggested experimental methods are coupled with effluent gas monitoring or electrochemical measurements (*operando* spectroscopy) will allow obtaining more fundamental information about these processes or other energy-related applications.

■ ASSOCIATED CONTENT

SI Supporting Information

The Supporting Information is available free of charge at <https://pubs.acs.org/doi/10.1021/acsaem.0c02675>.

Example Rietveld refinement of the CeO_2 sample, details of Raman band around 250 cm^{-1} , chemical expansion model, and water production during thermochemical cycling (PDF)

■ AUTHOR INFORMATION

Corresponding Author

J. L. M. Rupp – *Electrochemical Materials, Department of Materials Science and Engineering and Electrochemical Materials, Department of Electrical Engineering and Computer Science, Massachusetts Institute of Technology, Cambridge, Massachusetts 02139, United States*; orcid.org/0000-0001-7160-0108; Email: jrupp@mit.edu

Authors

- E. Sediva – *Electrochemical Materials, Department of Materials Science and Engineering, Massachusetts Institute of Technology, Cambridge, Massachusetts 02139, United States*; *Electrochemical Materials, ETHZ Department of Materials, 8093 Zürich, Switzerland*; orcid.org/0000-0002-9991-5790
- A. J. Carrillo – *Electrochemical Materials, Department of Materials Science and Engineering, Massachusetts Institute of Technology, Cambridge, Massachusetts 02139, United States*; orcid.org/0000-0002-5576-9277
- C. E. Halloran – *Electrochemical Materials, Department of Materials Science and Engineering, Massachusetts Institute of Technology, Cambridge, Massachusetts 02139, United States*

Complete contact information is available at: <https://pubs.acs.org/10.1021/acsaem.0c02675>

Author Contributions

E.S., A.J.C., and C.H. contributed equally to the work and should be considered co-first authors. A.J.C. and J.L.M.R. conceived the project. C.H. synthesized the materials. C.H., E.S., and A.J.C. performed the Raman tests. C.H. and E.S. made the Raman spectra fitting, analyses, and interpretation. E.S. developed the chemical expansion model. A.J.C. performed the XRD analyses and reactor tests. J.L.M.R. supervised the work. All the authors contributed to writing the manuscript and discussions about experiments and the resulting data.

Notes

The authors declare no competing financial interest.

■ ACKNOWLEDGMENTS

C.H. thanks the MIT Energy Initiative Undergraduate Research Opportunities Program for financial support. A.J.C. thanks the support of the MIT Eni Energy Fellowship 2018–2019. J.L.M.R. thanks the Thomas Lord Foundation for financial support. E.S. and J.L.M.R. thank the support of the Swiss National Science Foundation (Grant 155986/1). This work made use of the MRSEC Shared Experimental Facilities at MIT, supported by the National Science Foundation under Award DMR-14-19807. A.J.C. expresses his gratitude to Dr. A. Nenning and Dr. A. H. Bork for fruitful initial discussions on *in situ* redox Raman spectroscopy that greatly helped in the achievement of this work.

■ REFERENCES

- (1) Tuller, H. L. Solar to Fuels Conversion Technologies: A Perspective. *Mater. Renew. Sustain. Energy* **2017**, *6* (1), 3.
- (2) Romero, M.; Steinfeld, A. Concentrating Solar Thermal Power and Thermochemical Fuels. *Energy Environ. Sci.* **2012**, *5* (11), 9234–9245.
- (3) Kubicek, M.; Bork, A. H.; Rupp, J. L. M. Perovskite Oxides - a Review on a Versatile Material Class for Solar-to-Fuel Conversion Processes. *J. Mater. Chem. A* **2017**, *5* (24), 11983–12000.
- (4) Chueh, W. C.; Falter, C.; Abbott, M.; Scipio, D.; Furler, P.; Haile, S. M.; Steinfeld, A. High-Flux Solar-Driven Thermochemical Dissociation of CO_2 and H_2O Using Nonstoichiometric Ceria. *Science* **2010**, *330* (6012), 1797–1801.
- (5) Carrillo, R. J.; Scheffe, J. R. Advances and Trends in Redox Materials for Solar Thermochemical Fuel Production. *Sol. Energy* **2017**, *156*, 3–20.
- (6) Scheffe, J. R.; Steinfeld, A. Oxygen Exchange Materials for Solar Thermochemical Splitting of H_2O and CO_2 : A Review. *Mater. Today* **2014**, *17* (7), 341–348.
- (7) Li, S.; Wheeler, V. M.; Kreider, P. B.; Lipiński, W. Thermodynamic Analyses of Fuel Production via Solar-Driven Non-Stoichiometric Metal Oxide Redox Cycling. Part 1. Revisiting Flow and Equilibrium Assumptions. *Energy Fuels* **2018**, *32* (10), 10838–10847.
- (8) Bhosale, R. R.; Takalkar, G.; Sutar, P.; Kumar, A.; AlMomani, F.; Khrasheh, M. A Decade of Ceria Based Solar Thermochemical $\text{H}_2\text{O}/\text{CO}_2$ Splitting Cycle. *Int. J. Hydrogen Energy* **2019**, *44* (1), 34–60.
- (9) Marxer, D.; Furler, P.; Scheffe, J.; Geerlings, H.; Falter, C.; Batteiger, V.; Sizmann, A.; Steinfeld, A. Demonstration of the Entire Production Chain to Renewable Kerosene via Solar Thermochemical Splitting of H_2O and CO_2 . *Energy Fuels* **2015**, *29* (5), 3241–3250.
- (10) Marxer, D.; Furler, P.; Takacs, M.; Steinfeld, A. Solar Thermochemical Splitting of CO_2 into Separate Streams of CO and O_2 with High Selectivity, Stability, Conversion, and Efficiency. *Energy Environ. Sci.* **2017**, *10* (5), 1142–1149.
- (11) Gao, X.; Vidal, A.; Bayon, A.; Bader, R.; Hinkley, J.; Lipiński, W.; Tricoli, A. Efficient Ceria Nanostructures for Enhanced Solar Fuel Production via High-Temperature Thermochemical Redox Cycles. *J. Mater. Chem. A* **2016**, *4* (24), 9614–9624.
- (12) Bork, A. H.; Carrillo, A. J.; Hood, Z. D.; Yildiz, B.; Rupp, J. L. M. Oxygen Exchange in Dual-Phase $\text{La}_{0.65}\text{Sr}_{0.35}\text{MnO}_3\text{-CeO}_2$ Composites for Solar Thermochemical Fuel Production. *ACS Appl. Mater. Interfaces* **2020**, *12*, 32622.
- (13) Haessler, A.; Abanades, S.; Julbe, A.; Jouannaux, J.; Cartoixa, B. Two-Step CO_2 and H_2O Splitting Using Perovskite-Coated Ceria Foam for Enhanced Green Fuel Production in a Porous Volumetric Solar Reactor. *J. CO₂ Util.* **2020**, *41*, 101257.
- (14) Gao, X.; Liu, G.; Zhu, Y.; Kreider, P.; Bayon, A.; Gengenbach, T.; Lu, T.; Liu, Y.; Hinkley, J.; Lipiński, W.; Tricoli, A. Earth-Abundant Transition Metal Oxides with Extraordinary Reversible

Oxygen Exchange Capacity for Efficient Thermochemical Synthesis of Solar Fuels. *Nano Energy* **2018**, *50*, 347–358.

(15) Gao, X.; Di Bernardo, I.; Kreider, P.; Tran-Phu, T.; Cai, X.; Wang, N.; Zhu, Y.; Venkataraman, M. B.; Lipton-Duffin, J.; Bayon, A.; Lipiński, W.; Tricoli, A. Lattice Expansion in Optimally Doped Manganese Oxide: An Effective Structural Parameter for Enhanced Thermochemical Water Splitting. *ACS Catal.* **2019**, *9* (11), 9880–9890.

(16) Riaz, A.; Ali, M. U.; Lipiński, W.; Lowe, A. Enhanced Oxygen Exchange Capacity in Nano-Structured Vanadia-Ceria Multi-Phase Oxygen Carriers for Solar Thermal Fuel Production. *J. Mater. Chem. A* **2019**, *7* (48), 27347–27360.

(17) Riaz, A.; Ali, M. U.; Enge, T. G.; Tsuzuki, T.; Lowe, A.; Lipiński, W. Concentration-Dependent Solar Thermochemical CO₂/H₂O Splitting Performance by Vanadia-Ceria Multiphase Metal Oxide Systems; <https://spj.sciencemag.org/journals/research/2020/3049534/> (accessed 2020-12-22).

(18) Jacot, R.; Naik, J. M.; Moré, R.; Michalsky, R.; Steinfeld, A.; Patzke, G. R. Reactive Stability of Promising Scalable Doped Ceria Materials for Thermochemical Two-Step CO₂ Dissociation. *J. Mater. Chem. A* **2018**, *6* (14), 5807–5816.

(19) Arifin, D.; Ambrosini, A.; Wilson, S. A.; Mandal, B.; Muhich, C. L.; Weimer, A. W. Investigation of Zr, Gd/Zr, and Pr/Zr - Doped Ceria for the Redox Splitting of Water. *Int. J. Hydrogen Energy* **2020**, *45* (1), 160–174.

(20) McDaniel, A. H. Renewable Energy Carriers Derived from Concentrating Solar Power and Nonstoichiometric Oxides. *Curr. Opin. Green Sustain. Chem.* **2017**, *4*, 37–43.

(21) Takacs, M.; Scheffe, J. R.; Steinfeld, A. Oxygen Nonstoichiometry and Thermodynamic Characterization of Zr Doped Ceria in the 1573–1773 K Temperature Range. *Phys. Chem. Chem. Phys.* **2015**, *17* (12), 7813–7822.

(22) Zhao, Z.; Uddi, M.; Tsvetkov, N.; Yildiz, B.; Ghoniem, A. F. Redox Kinetics and Nonstoichiometry of Ce_{0.5}Zr_{0.5}O_{2-δ} for Water Splitting and Hydrogen Production. *J. Phys. Chem. C* **2017**, *121* (21), 11055–11068.

(23) Zhao, Z.; Uddi, M.; Tsvetkov, N.; Yildiz, B.; Ghoniem, A. F. Enhanced Intermediate-Temperature CO₂ Splitting Using Nonstoichiometric Ceria and Ceria-Zirconia. *Phys. Chem. Chem. Phys.* **2017**, *19* (37), 25774–25785.

(24) Scheffe, J. R.; Jacot, R.; Patzke, G. R.; Steinfeld, A. Synthesis, Characterization, and Thermochemical Redox Performance of Hf⁴⁺, Zr⁴⁺, and Sc³⁺ Doped Ceria for Splitting CO₂. *J. Phys. Chem. C* **2013**, *117* (46), 24104–24114.

(25) Petkovich, N. D.; Rudisill, S. G.; Venstrom, L. J.; Boman, D. B.; Davidson, J. H.; Stein, A. Control of Heterogeneity in Nanostructured Ce_{1-x}Zr_xO₂ Binary Oxides for Enhanced Thermal Stability and Water Splitting Activity. *J. Phys. Chem. C* **2011**, *115* (43), 21022–21033.

(26) Jacot, R.; Moré, R.; Michalsky, R.; Steinfeld, A.; Patzke, G. R. Trends in the Phase Stability and Thermochemical Oxygen Exchange of Ceria Doped with Potentially Tetravalent Metals. *J. Mater. Chem. A* **2017**, *5* (37), 19901–19913.

(27) Schmitt, R.; Nanning, A.; Kraynis, O.; Korobko, R.; Frenkel, A. I.; Lubomirsky, I.; Haile, S. M.; Rupp, J. L. M. A Review of Defect Structure and Chemistry in Ceria and Its Solid Solutions. *Chem. Soc. Rev.* **2020**, *49*, 554–592.

(28) Nakajima, A.; Yoshihara, A.; Ishigame, M. Defect-Induced Raman Spectra in Doped CeO₂. *Phys. Rev. B: Condens. Matter Mater. Phys.* **1994**, *50* (18), 13297–13307.

(29) McBride, J. R.; Hass, K. C.; Poindexter, B. D.; Weber, W. H. Raman and X-ray Studies of Ce_{1-x}RE_xO_{2-y}, Where RE = La, Pr, Nd, Eu, Gd, and Tb. *J. Appl. Phys.* **1994**, *76* (4), 2435–2441.

(30) Lee, Y.; He, G.; Akey, A. J.; Si, R.; Flytzani-Stephanopoulos, M.; Herman, I. P. Raman Analysis of Mode Softening in Nanoparticle CeO_{2-δ} and Au-CeO_{2-δ} during CO Oxidation. *J. Am. Chem. Soc.* **2011**, *133* (33), 12952–12955.

(31) Li, L.; Chen, F.; Lu, J.-Q.; Luo, M.-F. Study of Defect Sites in Ce_{1-x}M_xO_{2-δ} (x = 0.2) Solid Solutions Using Raman Spectroscopy. *J. Phys. Chem. A* **2011**, *115* (27), 7972–7977.

(32) Solís, C.; Balaguer, M.; Serra, J. M. In Situ Raman Characterization of SOFC Materials in Operational Conditions: A Doped Ceria Study. *Membranes* **2020**, *10* (7), 148.

(33) Guo, M.; Lu, J.; Wu, Y.; Wang, Y.; Luo, M. UV and Visible Raman Studies of Oxygen Vacancies in Rare-Earth-Doped Ceria. *Langmuir* **2011**, *27* (7), 3872–3877.

(34) Taniguchi, T.; Watanabe, T.; Sugiyama, N.; Subramani, A. K.; Wagata, H.; Matsushita, N.; Yoshimura, M. Identifying Defects in Ceria-Based Nanocrystals by UV Resonance Raman Spectroscopy. *J. Phys. Chem. C* **2009**, *113* (46), 19789–19793.

(35) Pu, Z.-Y.; Lu, J.-Q.; Luo, M.-F.; Xie, Y.-L. Study of Oxygen Vacancies in Ce_{0.9}Pr_{0.1}O_{2-δ} Solid Solution by in Situ X-Ray Diffraction and in Situ Raman Spectroscopy. *J. Phys. Chem. C* **2007**, *111* (50), 18695–18702.

(36) Shimanouchi, T.; Tsuboi, M.; Miyazawa, T. Optically Active Lattice Vibrations as Treated by the GF-Matrix Method. *J. Chem. Phys.* **1961**, *35* (5), 1597–1612.

(37) Hernández, W. Y.; Romero-Sarria, F.; Centeno, M. A.; Odriozola, J. A. In Situ Characterization of the Dynamic Gold-Support Interaction over Ceria Modified Eu³⁺. Influence of the Oxygen Vacancies on the CO Oxidation Reaction. *J. Phys. Chem. C* **2010**, *114* (24), 10857–10865.

(38) Carrillo, A. J.; Bork, A. H.; Moser, T.; Sediva, E.; Hood, Z. D.; Rupp, J. L. M. Modifying La_{0.6}Sr_{0.4}MnO₃ Perovskites with Cr Incorporation for Fast Isothermal CO₂-Splitting Kinetics in Solar-Driven Thermochemical Cycles. *Adv. Energy Mater.* **2019**, *9* (28), 1803886.

(39) Zhao, Z.; Uddi, M.; Tsvetkov, N.; Yildiz, B.; Ghoniem, A. F. Redox Kinetics Study of Fuel Reduced Ceria for Chemical-Looping Water Splitting. *J. Phys. Chem. C* **2016**, *120* (30), 16271–16289.

(40) Krenzke, P. T.; Fosheim, J. R.; Davidson, J. H. Solar Fuels via Chemical-Looping Reforming. *Sol. Energy* **2017**, *156*, 48–72.

(41) Maiti, D.; Hare, B. J.; Daza, Y. A.; Ramos, A. E.; Kuhn, J. N.; Bhethanabotla, V. R. Earth Abundant Perovskite Oxides for Low Temperature CO₂ Conversion. *Energy Environ. Sci.* **2018**, *11* (3), 648–659.

(42) Krenzke, P. T.; Fosheim, J. R.; Zheng, J.; Davidson, J. H. Synthesis Gas Production via the Solar Partial Oxidation of Methane-Ceria Redox Cycle: Conversion, Selectivity, and Efficiency. *Int. J. Hydrogen Energy* **2016**, *41* (30), 12799–12811.

(43) Ackermann, S.; Sauvin, L.; Castiglioni, R.; Rupp, J. L. M.; Scheffe, J. R.; Steinfeld, A. Kinetics of CO₂ Reduction over Nonstoichiometric Ceria. *J. Phys. Chem. C* **2015**, *119* (29), 16452–16461.

(44) Le Gal, A.; Abanades, S. Dopant Incorporation in Ceria for Enhanced Water-Splitting Activity during Solar Thermochemical Hydrogen Generation. *J. Phys. Chem. C* **2012**, *116* (25), 13516–13523.

(45) Jiang, Q.; Zhou, G.; Jiang, Z.; Li, C. Thermochemical CO₂ Splitting Reaction with Ce_xM_{1-x}O_{2-δ} (M = Ti⁴⁺, Sn⁴⁺, Hf⁴⁺, Zr⁴⁺, La³⁺, Y³⁺ and Sm³⁺) Solid Solutions. *Sol. Energy* **2014**, *99*, 55–66.

(46) Shannon, R. D.; Prewitt, C. T. Effective Ionic Radii in Oxides and Fluorides. *Acta Crystallogr., Sect. B: Struct. Crystallogr. Cryst. Chem.* **1969**, *25* (5), 925–946.

(47) Muhich, C.; Steinfeld, A. Principles of Doping Ceria for the Solar Thermochemical Redox Splitting of H₂O and CO₂. *J. Mater. Chem. A* **2017**, *5* (30), 15578–15590.

(48) Call, F.; Roeb, M.; Schmücker, M.; Sattler, C.; Pitz-Paal, R. Ceria Doped with Zirconium and Lanthanide Oxides to Enhance Solar Thermochemical Production of Fuels. *J. Phys. Chem. C* **2015**, *119* (13), 6929–6938.

(49) Meng, Q.-L.; Lee, C.; Ishihara, T.; Kaneko, H.; Tamura, Y. Reactivity of CeO₂-Based Ceramics for Solar Hydrogen Production via a Two-Step Water-Splitting Cycle with Concentrated Solar Energy. *Int. J. Hydrogen Energy* **2011**, *36* (21), 13435–13441.

(50) Hoes, M.; Muhich, C. L.; Jacot, R.; Patzke, G. R.; Steinfeld, A. Thermodynamics of Paired Charge-Compensating Doped Ceria with Superior Redox Performance for Solar Thermochemical Splitting of H₂O and CO₂. *J. Mater. Chem. A* **2017**, *5* (36), 19476–19484.

- (51) Lu, Y.; Zhu, L.; Agrafiotis, C.; Vieten, J.; Roeb, M.; Sattler, C. Solar Fuels Production: Two-Step Thermochemical Cycles with Cerium-Based Oxides. *Prog. Energy Combust. Sci.* **2019**, *75*, 100785.
- (52) Schilling, C.; Hofmann, A.; Hess, C.; Ganduglia-Pirovano, M. V. Raman Spectra of Polycrystalline CeO₂: A Density Functional Theory Study. *J. Phys. Chem. C* **2017**, *121* (38), 20834–20849.
- (53) Reddy, B. M.; Bharali, P.; Saikia, P.; Park, S.-E.; van den Berg, M. W. E.; Muhler, M.; Grünert, W. Structural Characterization and Catalytic Activity of Nanosized Ce_xM_{1-x}O₂ (M = Zr and Hf) Mixed Oxides. *J. Phys. Chem. C* **2008**, *112* (31), 11729–11737.
- (54) Loridant, S. Raman Spectroscopy as a Powerful Tool to Characterize Ceria-Based Catalysts. *Catal. Today* **2020**, DOI: 10.1016/j.cattod.2020.03.044.
- (55) Marrocchelli, D.; Bishop, S. R.; Tuller, H. L.; Yildiz, B. Understanding Chemical Expansion in Non-Stoichiometric Oxides: Ceria and Zirconia Case Studies. *Adv. Funct. Mater.* **2012**, *22* (9), 1958–1965.
- (56) Artini, C.; Pani, M.; Carnasciali, M. M.; Buscaglia, M. T.; Plaisier, J. R.; Costa, G. A. Structural Features of Sm- and Gd-Doped Ceria Studied by Synchrotron X-Ray Diffraction and μ -Raman Spectroscopy. *Inorg. Chem.* **2015**, *54* (8), 4126–4137.
- (57) Sediva, E.; Defferriere, T.; Perry, N. H.; Tuller, H. L.; Rupp, J. L. M. In Situ Method Correlating Raman Vibrational Characteristics to Chemical Expansion via Oxygen Nonstoichiometry of Perovskite Thin Films. *Adv. Mater.* **2019**, *31*, 1902493.
- (58) Nakayama, M.; Ohshima, H.; Nogami, M.; Martin, M. A. Concerted Migration Mechanism of Mixed Oxide Ion and Electron Conduction in Reduced Ceria Studied by First-Principles Density Functional Theory. *Phys. Chem. Chem. Phys.* **2012**, *14* (17), 6079.
- (59) Bishop, S. R.; Duncan, K. L.; Wachsmann, E. D. Defect Equilibria and Chemical Expansion in Non-Stoichiometric Undoped and Gadolinium-Doped Cerium Oxide. *Electrochim. Acta* **2009**, *54* (5), 1436–1443.
- (60) Artini, C.; Carnasciali, M. M.; Plaisier, J. R.; Costa, G. A.; Pani, M. A Novel Method for the Evaluation of the Rare Earth (RE) Coordination Number in RE-Doped Ceria through Raman Spectroscopy. *Solid State Ionics* **2017**, *311*, 90–97.
- (61) Moncada, J.; Adams, W. R.; Thakur, R.; Julin, M.; Carrero, C. A. Developing a Raman Spectrokinetic Approach To Gain Insights into the Structure-Reactivity Relationship of Supported Metal Oxide Catalysts. *ACS Catal.* **2018**, *8* (10), 8976–8986.
- (62) Ober, P.; Rogg, S.; Hess, C. Direct Evidence for Active Support Participation in Oxide Catalysis: Multiple Operando Spectroscopy of VO_x/Ceria. *ACS Catal.* **2020**, *10* (5), 2999–3008.
- (63) Wu, X.-Y.; Ghoniem, A. F. Mixed Ionic-Electronic Conducting (MIEC) Membranes for Thermochemical Reduction of CO₂: A Review. *Prog. Energy Combust. Sci.* **2019**, *74*, 1–30.
- (64) Carrillo, A. J.; Kim, K. J.; Hood, Z. D.; Bork, A. H.; Rupp, J. L. M. La_{0.6}Sr_{0.4}Cr_{0.8}Co_{0.2}O₃ Perovskite Decorated with Exsolved Co Nanoparticles for Stable CO₂ Splitting and Syngas Production. *ACS Appl. Energy Mater.* **2020**, *3*, 4569.